

SUPPLEMENTARY MATERIAL

[NiFe]-Hydrogenase synthetic models with redox-active ligands

David Schilter,^{A,B,C} Danielle L. Gray,^B Amy L. Fuller,^B and Thomas B. Rauchfuss^B

^AIBS Center for Multidimensional Carbon Materials, 50 UNIST-gil, Ulsan 44919 (South Korea)

^BDepartment of Chemistry, University of Illinois at Urbana-Champaign, 600 S. Goodwin Ave. Urbana, IL 61801, USA

^CCorresponding author. Email: d.schilter@gmail.com

List of Figures

Figure S1. FT-IR spectrum (ν_{CO} region, CH ₂ Cl ₂) of [1a(μ -H)]BF ₄	2
Figure S2. ³¹ P{ ¹ H} NMR spectra (CD ₂ Cl ₂ , 202 MHz) of [1a(μ -H)]BF ₄	2
Figure S3. ¹ H NMR spectrum (CD ₂ Cl ₂ , 500 MHz) of [1a(μ -H)]BF ₄	3
Figure S4. Positive ion ESI mass spectrum of [1a(μ -H)]BF ₄	3
Figure S5. X-ray structure of [1a(μ -H)]BF ₄ ·CH ₂ Cl ₂	4
Figure S6. Cyclic voltammograms of [1a(μ -H)]BF ₄ acquired in the presence of varying molar equivalents of CF ₃ CO ₂ H.....	5
Figure S7. Analysis of the currents observed for reduction of [1a(μ -H)]BF ₄ in the presence of CF ₃ CO ₂ H.....	5
Figure S8. FT-IR spectrum (ν_{CO} region, CH ₂ Cl ₂) of [1a]BF ₄	6
Figure S9. Positive ion ESI mass spectrum of [1a]BF ₄	6
Figure S10. Cyclic voltammogram of [1a]BF ₄	7
Figure S11: FT-IR spectrum (ν_{CO} region, CH ₂ Cl ₂) of [1b]BF ₄	7
Figure S12: Positive ion ESI mass spectrum of [1b]BF ₄	8
Figure S13: FT-IR spectrum (ν_{CO} region, CH ₂ Cl ₂) of [1c]BF ₄	8
Figure S14. Positive ion ESI mass spectrum of [1c]BF ₄	9
Figure S15. X-band EPR spectra of [1c]BF ₄ in CH ₂ Cl ₂ /PhMe.....	9
Figure S16. Cyclic voltammogram of [1c]BF ₄	9
Figure S17. FT-IR spectrum (ν_{CO} region, CH ₂ Cl ₂) of [1c](BF ₄) ₂	10
Figure S18. ³¹ P{ ¹ H} NMR spectrum (CD ₂ Cl ₂ , 202 MHz) of [1c](BF ₄) ₂	10
Figure S19. ¹ H NMR spectrum (CD ₂ Cl ₂ , 500 MHz) of [1c](BF ₄) ₂	11
Figure S20: Positive ion ESI mass spectra of [1c](BF ₄) ₂	12
Figure S21. FT-IR spectrum (ν_{CO} region, CH ₂ Cl ₂) of [2a]BF ₄	13
Figure S22. Positive ion ESI mass spectrum of [2a]BF ₄	13
Figure S23. Cyclic voltammogram of [2a]BF ₄	13
Figure S24. FT-IR spectrum (ν_{CO} region, CH ₂ Cl ₂) of [2b]BF ₄	14
Figure S25. Positive ion ESI mass spectrum of [2b]BF ₄	14
Figure S26. Cyclic voltammogram of [2b]BF ₄	15
Figure S27: FT-IR spectrum (ν_{CO} region, CH ₂ Cl ₂) of [2c]BF ₄	15

Figure S28. Positive ion ESI mass spectrum of [2c]BF ₄	16
Figure S29. X-band EPR spectra of [2c]BF ₄ in CH ₂ Cl ₂ /PhMe	16
Figure S30. Cyclic voltammogram of [2c]BF ₄	16
Figure S31: FT-IR spectrum (ν_{CO} region, CH ₂ Cl ₂) of [3](BF ₄) ₂	17
Figure S32. Positive ion ESI mass spectrum of [3](BF ₄) ₂	17
Figure S33. X-band EPR spectra of [3](BF ₄) ₂ in CH ₂ Cl ₂ /PhMe	18
Figure S34. Cyclic voltammogram of [3](BF ₄) ₂	18

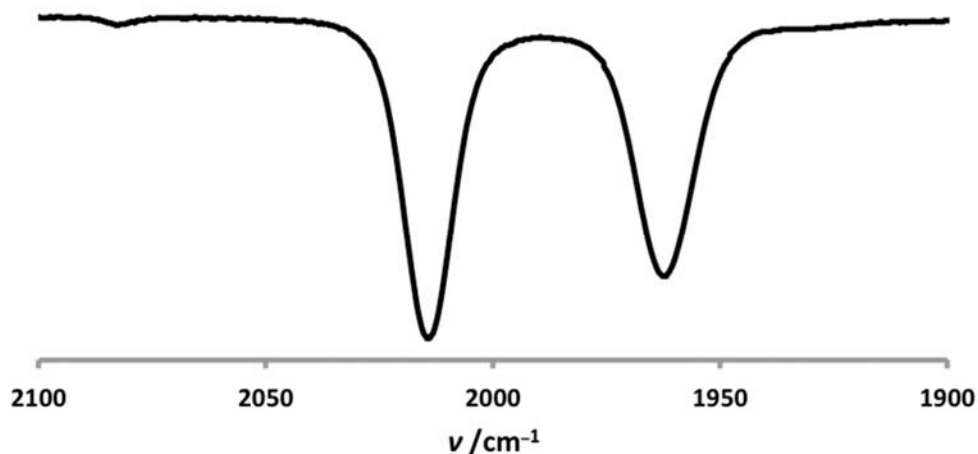


Figure S1. FT-IR spectrum (ν_{CO} region, CH₂Cl₂) of [1a(μ -H)]BF₄.

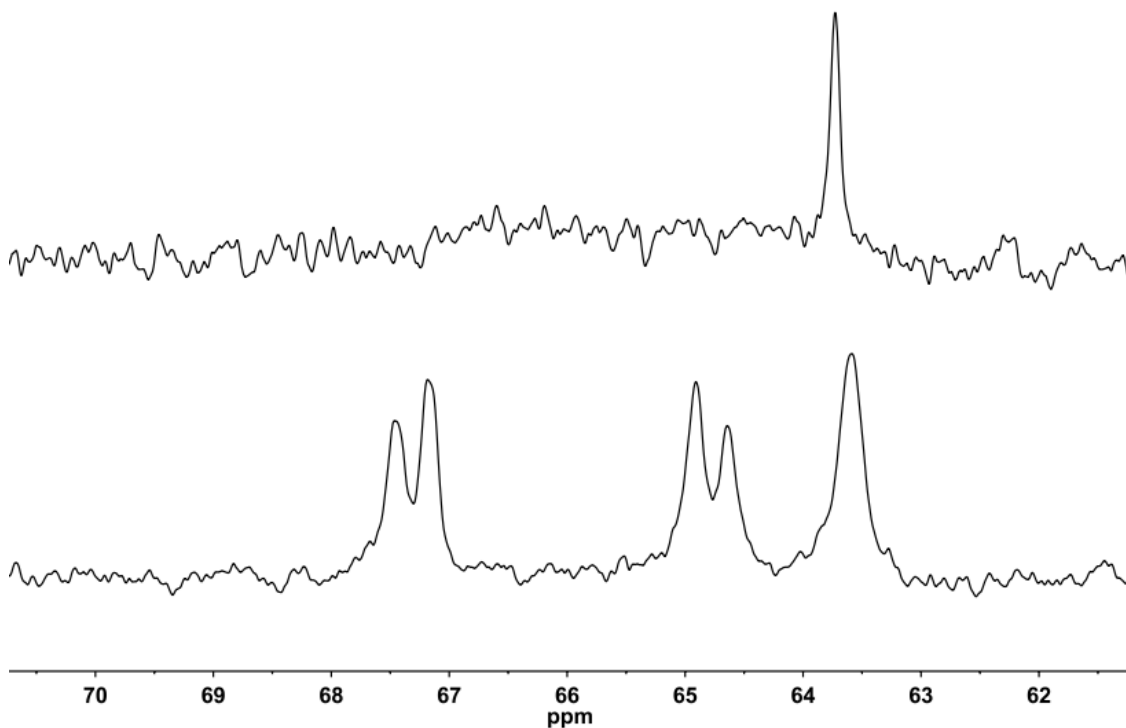


Figure S2. ³¹P{¹H} NMR spectra (CD₂Cl₂, 202 MHz) of [1a(μ -H)]BF₄ recorded at room temperature (top) and at -28°C (bottom).

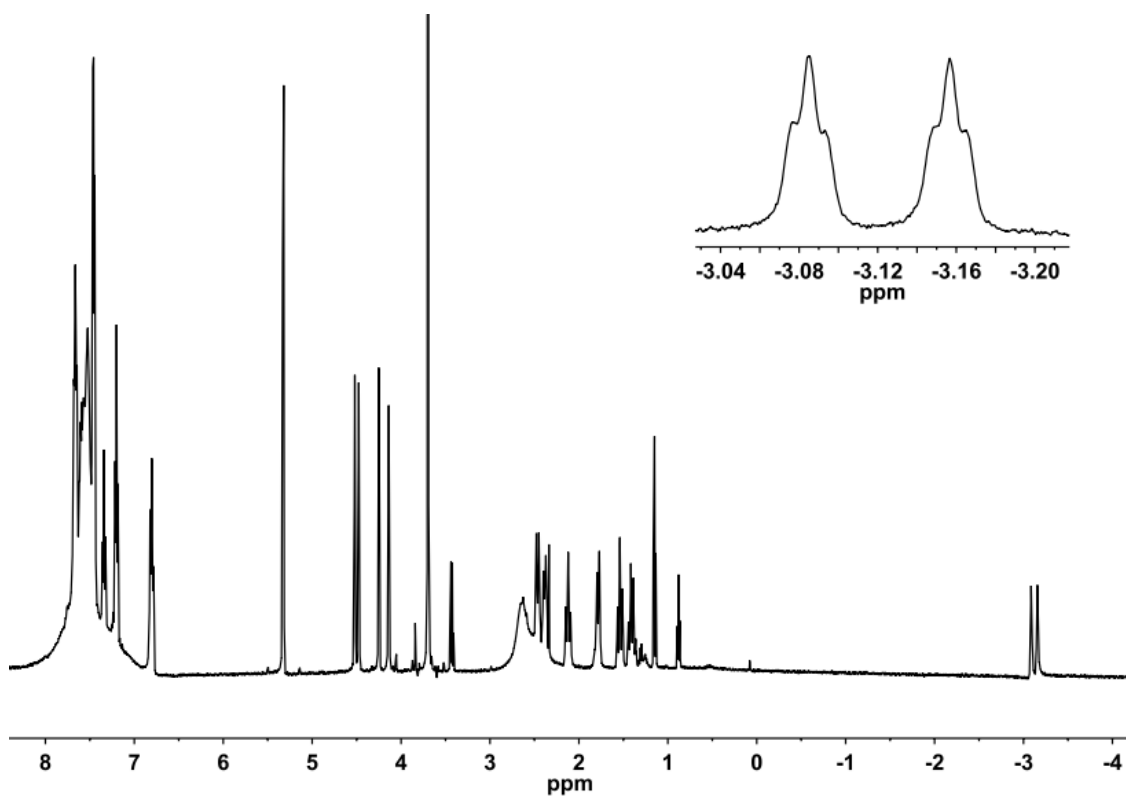


Figure S3. ^1H NMR spectrum (CD_2Cl_2 , 500 MHz) of $[\mathbf{1a}(\mu\text{-H})]\text{BF}_4$. Resonances at 3.43 (Et_2O), 1.31 (pentane), 1.12 (Et_2O) and 0.89 ppm (pentane) are from impurities in the NMR solvent.

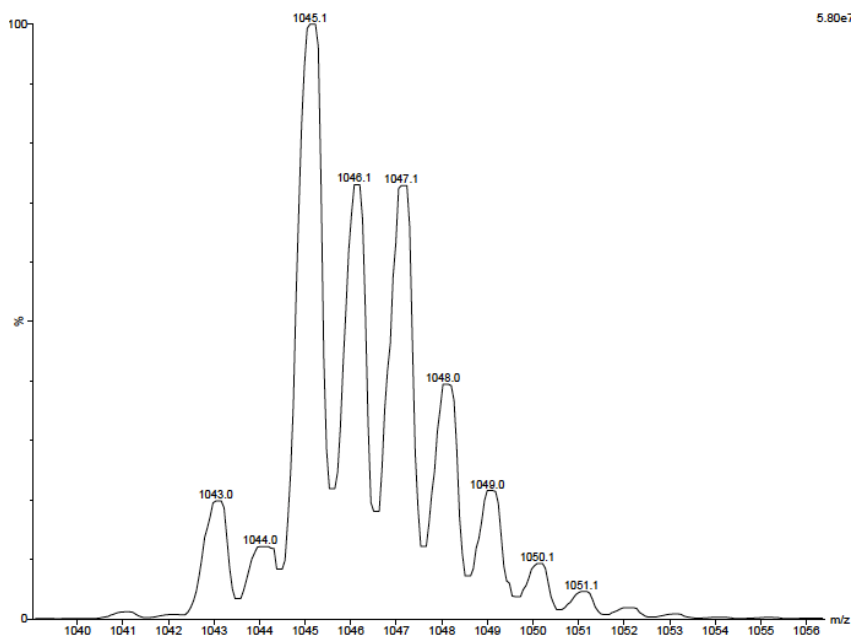


Figure S4. Positive ion ESI mass spectrum of $[\mathbf{1a}(\mu\text{-H})]\text{BF}_4$.

Brown single crystals of $[\mathbf{1a}(\mu\text{-H})]\text{BF}_4 \cdot \text{CH}_2\text{Cl}_2$ formed upon slow diffusion of pentane vapor into a concentrated CH_2Cl_2 solution of $[\mathbf{1a}(\mu\text{-H})]\text{BF}_4$. One crystal was subjected to X-ray diffraction at 173 K, its space group determined as monoclinic $P2_1/c$ ($Z = 4$) with cell parameters: a 12.6528(6) Å, b 33.7738(18) Å, c 12.2942(6) Å, α 90°, β 90.373(4)°, γ 90°. While these preliminary data were of poor quality, they did confirm the atom connectivity within the complex. The Ni-Fe distance in $[\mathbf{1a}(\mu\text{-H})]^+$ (2.662 Å) is similar to that in the analogous triphosphine hydride $[(\text{dppe})\text{Ni}(\text{pdt})\text{HFe}(\text{CO})_2(\text{PPh}_3)]^+$ (2.643 Å), with the monophosphine occupying a basal coordination site *trans* to an S atom in both complexes. The H^- ligand was not resolved in the Fourier difference map. Rather, it was fixed at a distance from Fe1 equivalent to that in the PPh_3 congener. Indirect evidence of the presence of H^- comes from the stereochemistry at the Fe1 site: were the hydride not present, then the mppf ligand would likely occupy an apical position, as it does in the Ni(II)Fe(I) model complexes of the type $[(\text{dppe})\text{Ni}(\text{pdt})\text{Fe}(\text{CO})_2(\text{PRAr}_2)]^+$, including $[\mathbf{2b}]^+$. In this case, the π -accepting CO ligands are poised *trans* to the π -donating CO groups, no doubt a favorable situation. But this is not the case with $[\mathbf{1a}(\mu\text{-H})]^+$, in which mppf occupied a basal site, ceding its favorable apical position to CO, a ligand that prefers a strong donor *trans* to it, in this case H^- . Lastly, it is noted that the bond distances are consistent with a Ni(II)($\mu\text{-H}$)Fe(II)Fe(II) description for this complex, in line with the CO stretching frequencies and the sharpness of the NMR data.

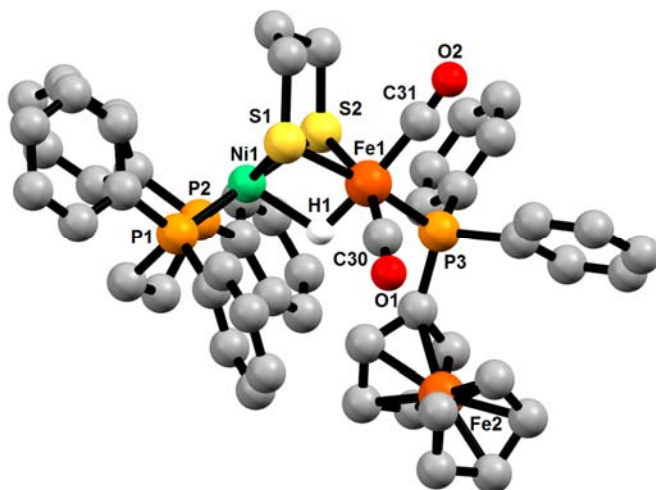


Figure S5. X-ray structure of $[\mathbf{1a}(\mu\text{-H})]\text{BF}_4 \cdot \text{CH}_2\text{Cl}_2$ with the H atoms, disordered BF_4^- anion and CH_2Cl_2 solvate molecule omitted for clarity. Disorder in the Cp ring and two Ph groups of the dppe ligand is also omitted for clarity. Selected distances (Å): Ni1-Fe1, 2.66; Ni1-P1, 2.17; Ni1-P2, 2.17; Ni1-S1, 2.21; Ni1-S2, 2.21; Fe1-S1, 2.31; Fe1-S2, 2.31; Fe1-H1, 1.49; Fe1-C30, 1.79; Fe1-C31, 1.78; Fe1-P3, 2.23; Fe2-C₅H₅(centroid), 1.64; Fe2-C₅H₄PPh₂(centroid), 1.72.

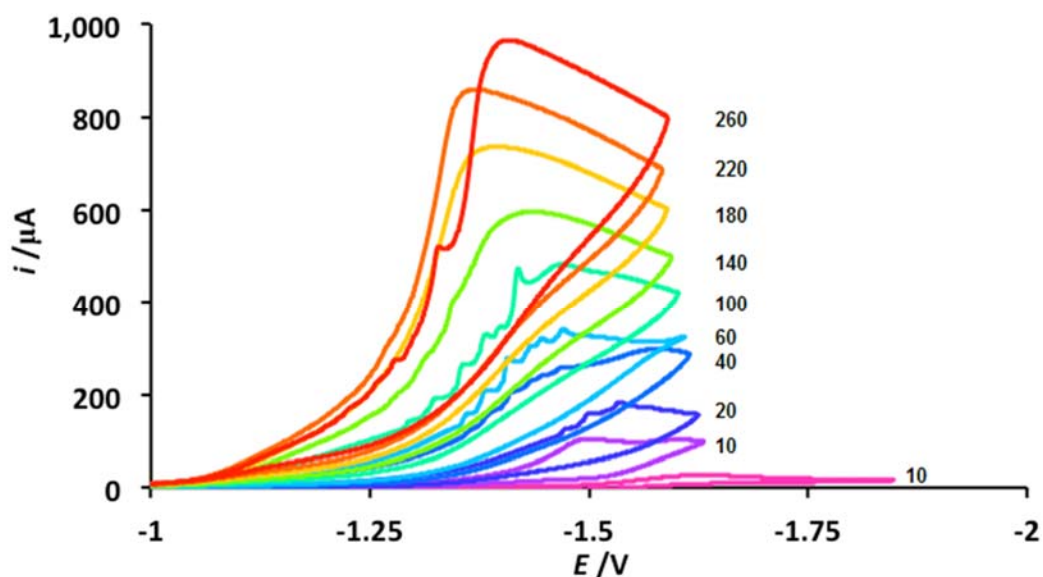


Figure S6. Cyclic voltammograms of [1a(μ-H)]BF₄ (1 mM) acquired in the presence of varying molar equivalents of CF₃CO₂H.

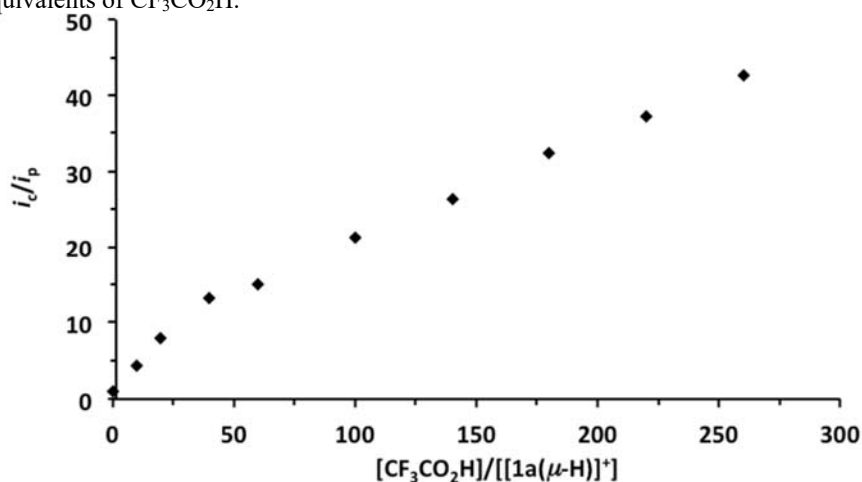


Figure S7. Analysis of the currents observed for reduction of [1a(μ-H)]BF₄ (1 mM). The quotient of the current in the presence (i_c) to that in the absence of the acid CF₃CO₂H (i_p) is plotted against the molar ratio of CF₃CO₂H to [1a(μ-H)]⁺. At higher acid concentrations, the wave shifts to more negative potentials, in line with direct reduction of CF₃CO₂H at the glassy carbon electrode.

The turnover frequency k for catalytic hydrogen evolution ($n = 2$) at a given scan rate ν and temperature T can be determined using peak currents in the presence (i_c) and absence of acid (i_p). For catalysis at $E_{pc} = -1.37$ V (potential at $i_c/2 = E_{pc} = -1.33$ V):

$$\frac{i_c}{i_p} = \frac{n}{0.4463} \sqrt{\frac{RTk}{F\nu}}$$

$$\frac{965 \mu A}{22.6 \mu A} = \frac{2}{0.4463} \sqrt{\frac{(8.314 \text{ JK}^{-1}\text{mol}^{-1})(298 \text{ K})k}{(96485 \text{ Cmol}^{-1})(0.1 \text{ JC}^{-1}\text{s}^{-1})}}$$

$$k \approx 350 \text{ s}^{-1}$$

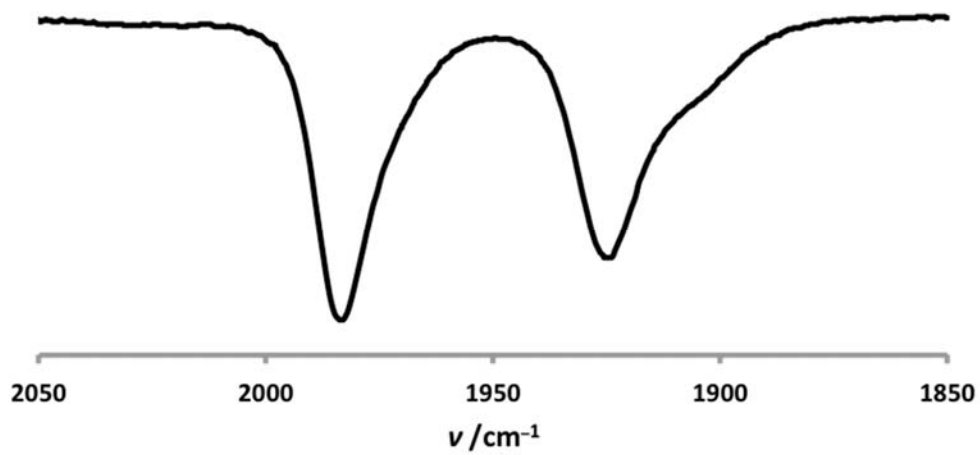


Figure S8. FT-IR spectrum (ν_{CO} region, CH_2Cl_2) of **[1a]** BF_4 .

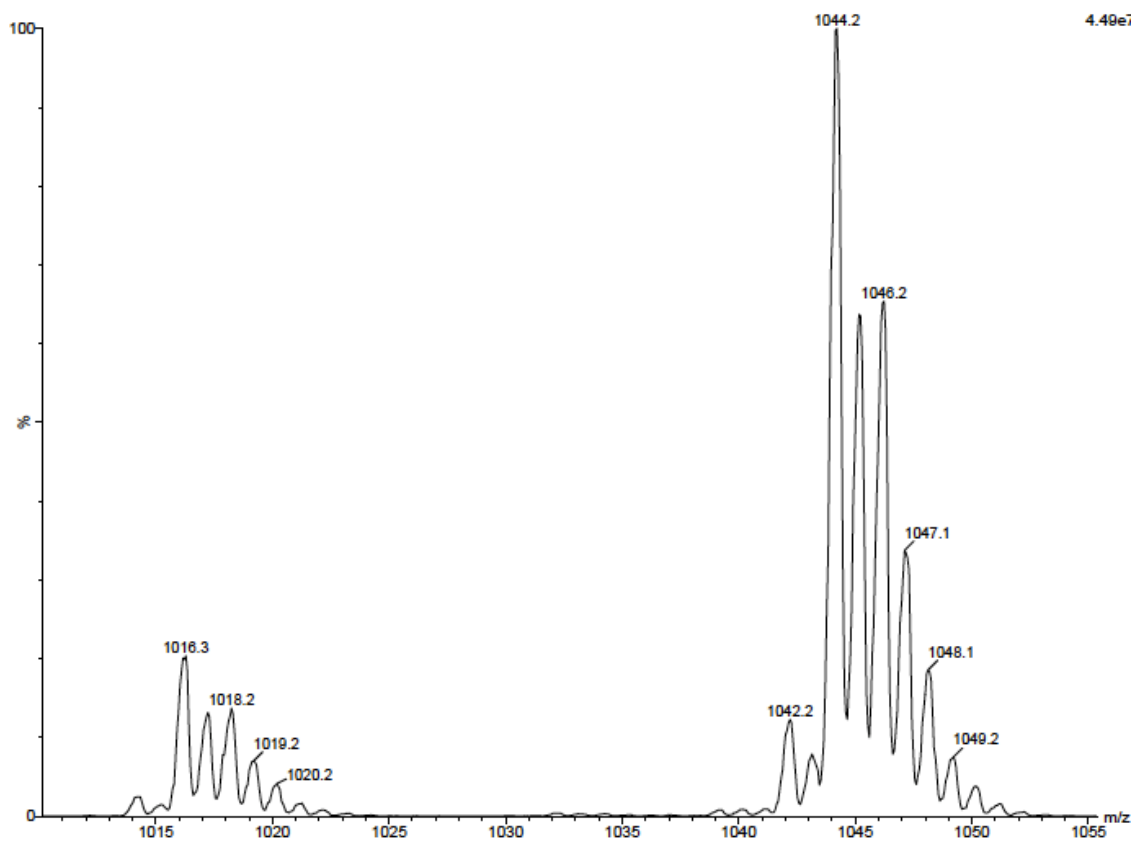


Figure S9. Positive ion ESI mass spectrum of **[1a]** BF_4 .

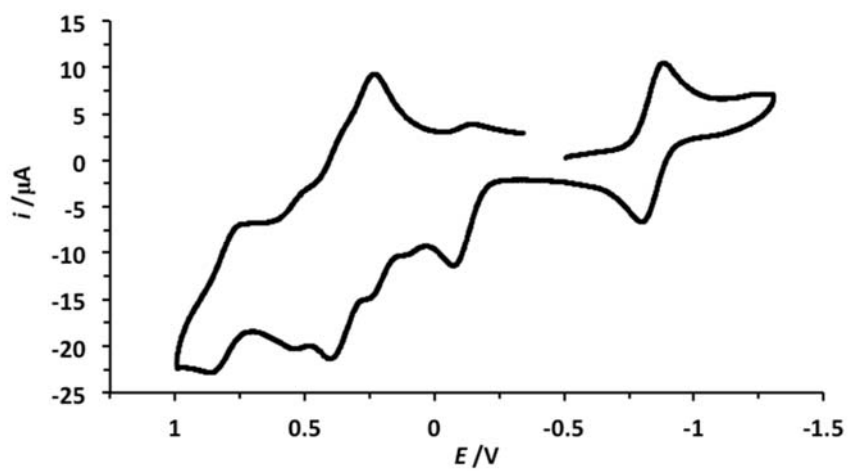


Figure S10. Cyclic voltammogram of [1a]BF₄.

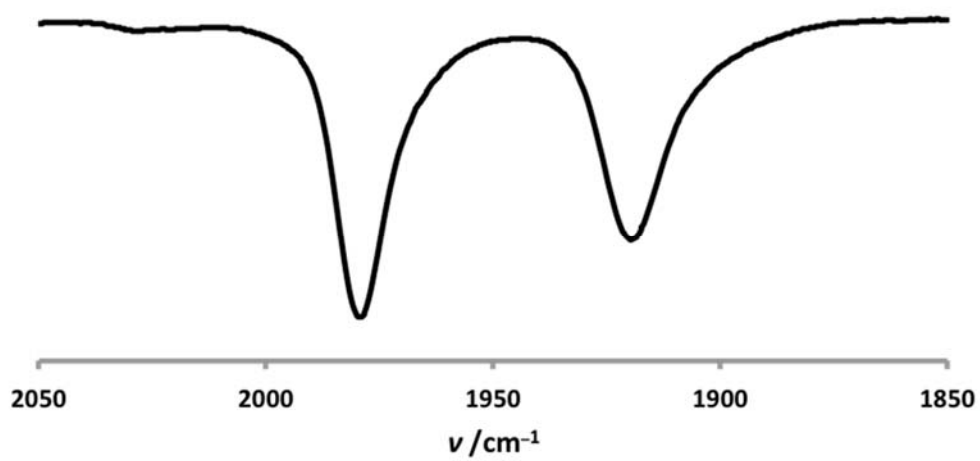


Figure S11: FT-IR spectrum (ν_{CO} region, CH₂Cl₂) of [1b]BF₄.

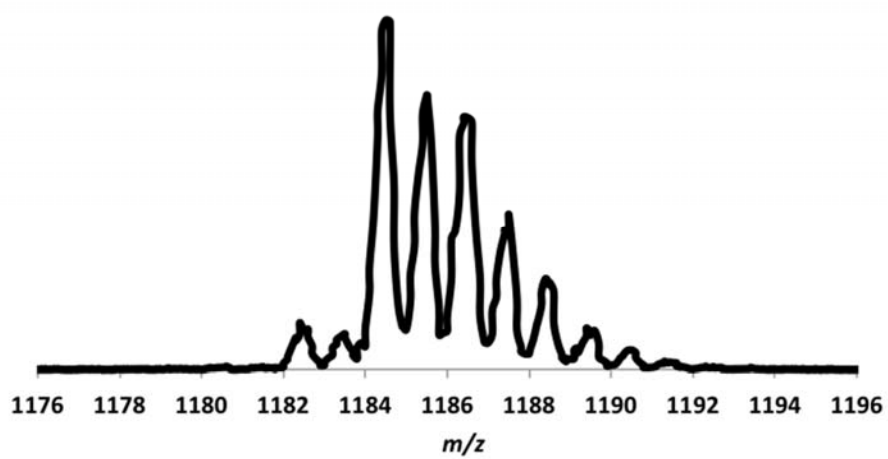


Figure S12: Positive ion ESI mass spectrum of [1b]BF₄.

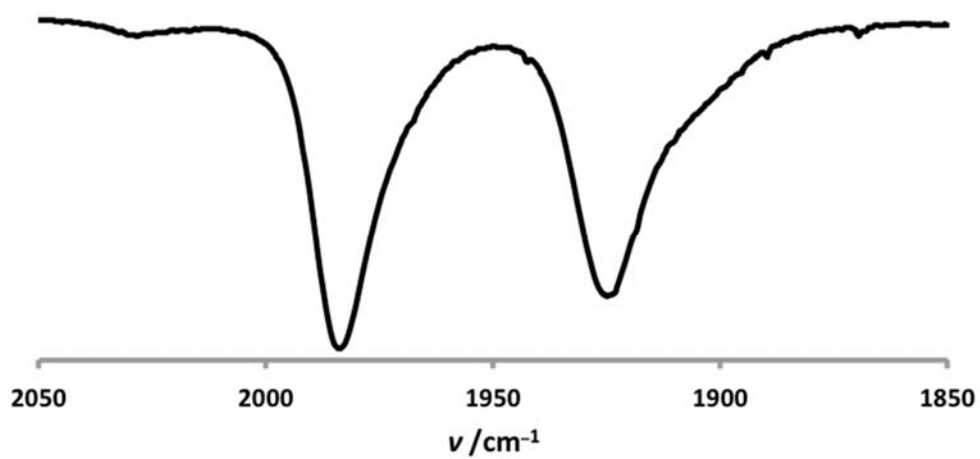


Figure S13: FT-IR spectrum (ν_{CO} region, CH₂Cl₂) of [1c]BF₄.

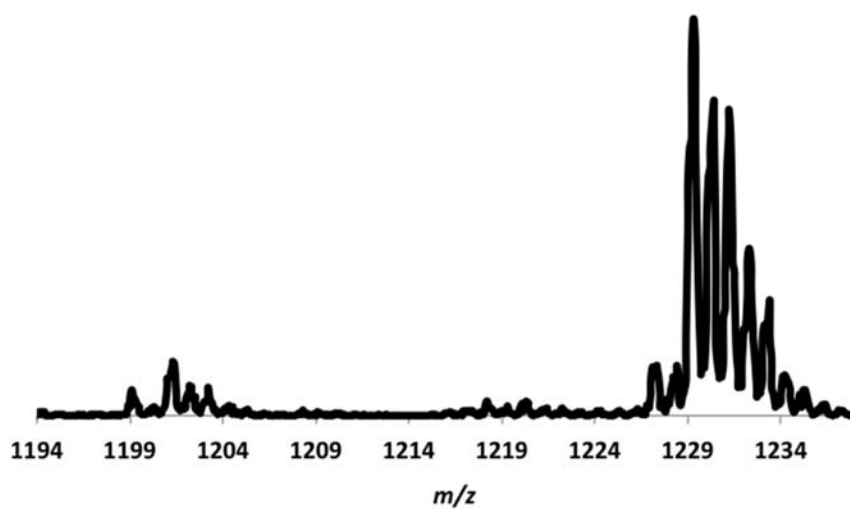


Figure S14. Positive ion ESI mass spectrum of [1c]BF₄.

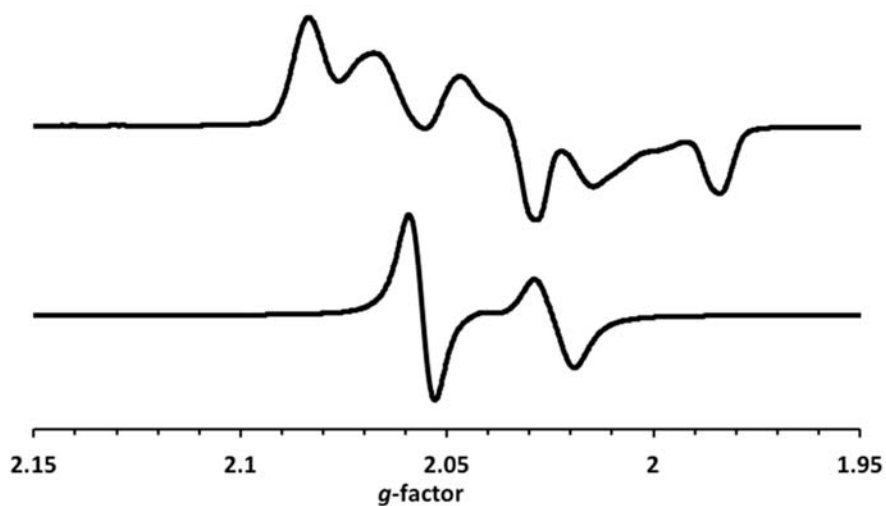


Figure S15. X-band EPR spectra of [1c]BF₄ in CH₂Cl₂/PhMe recorded at 110 K (top) and room temperature (bottom).

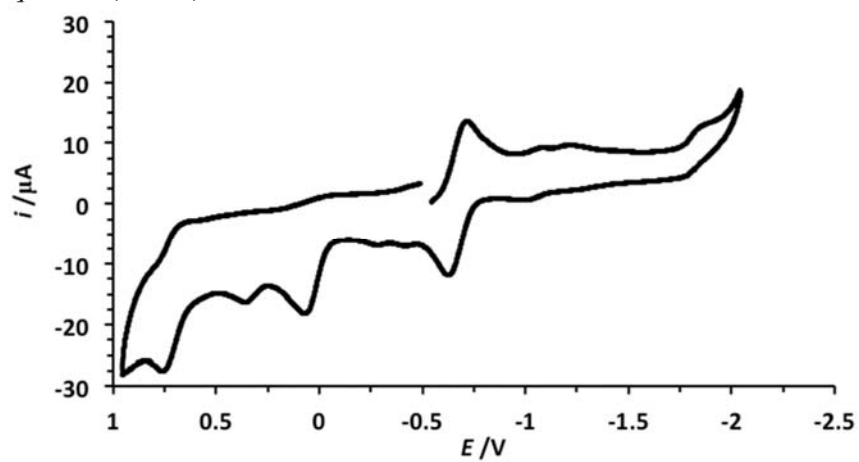


Figure S16. Cyclic voltammogram of [1c]BF₄.

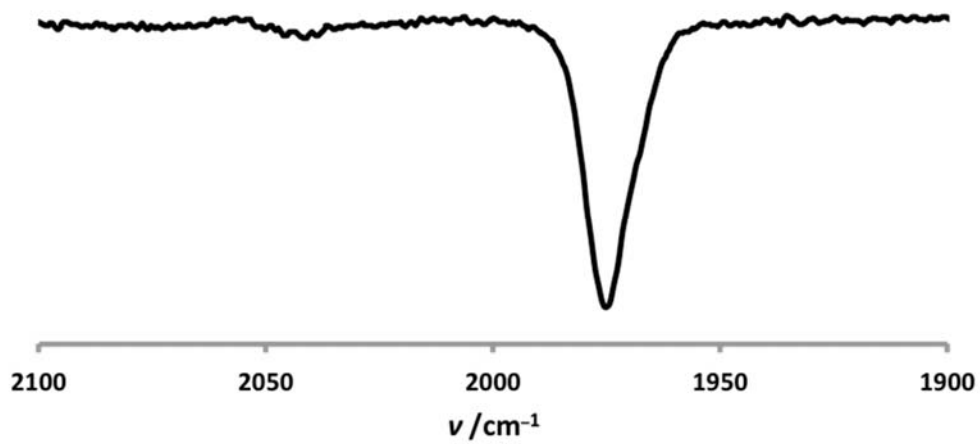


Figure S17. FT-IR spectrum (ν_{CO} region, CH_2Cl_2) of $[\mathbf{1c}](\text{BF}_4)_2$.

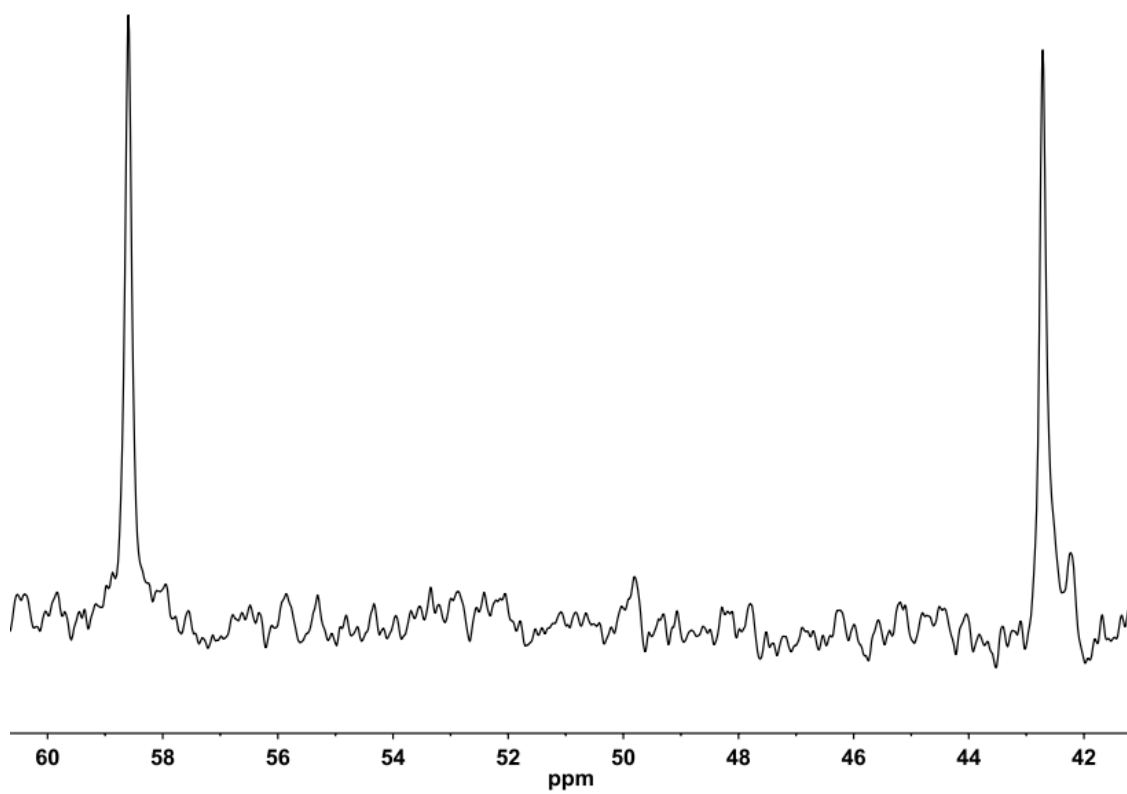


Figure S18. $^{31}\text{P}\{^1\text{H}\}$ NMR spectrum (CD_2Cl_2 , 202 MHz) of $[\mathbf{1c}](\text{BF}_4)_2$.

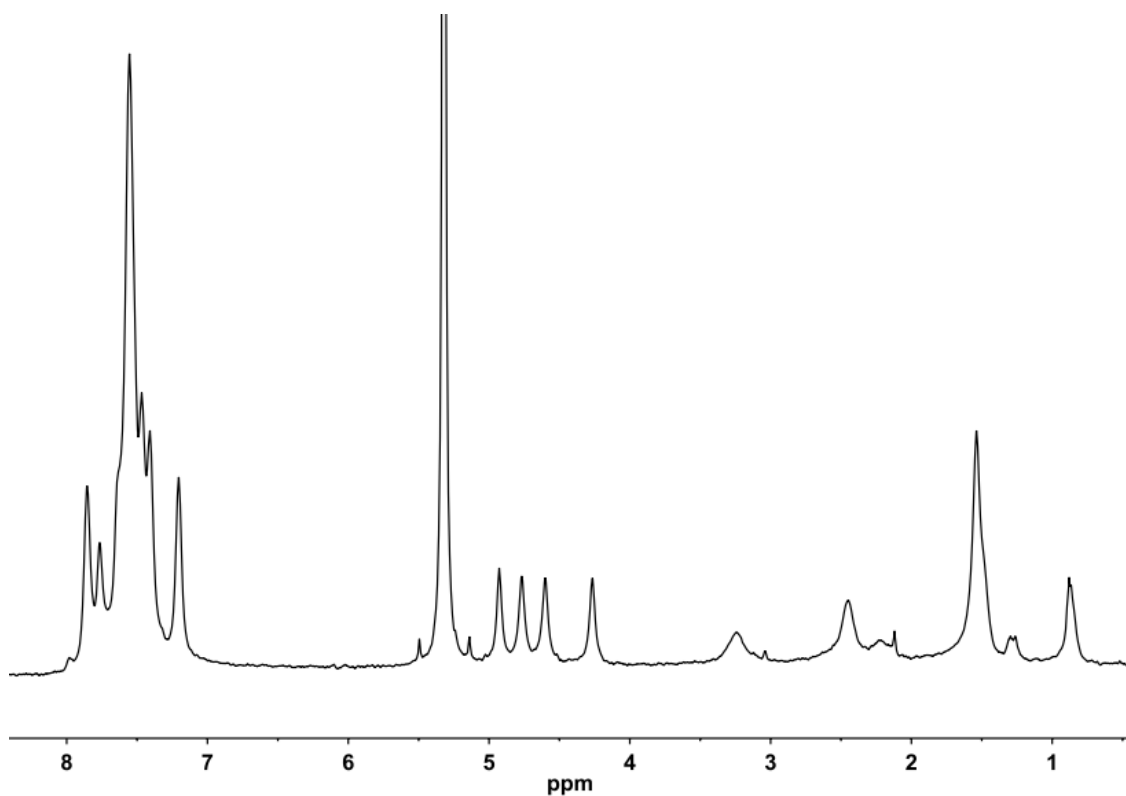


Figure S19. ^1H NMR spectrum (CD_2Cl_2 , 500 MHz) of $[\mathbf{1c}](\text{BF}_4)_2$. Resonances at 3.43 (Et_2O), 1.31 (pentane), 1.12 (Et_2O) and 0.89 ppm (pentane) are from impurities in the NMR solvent.

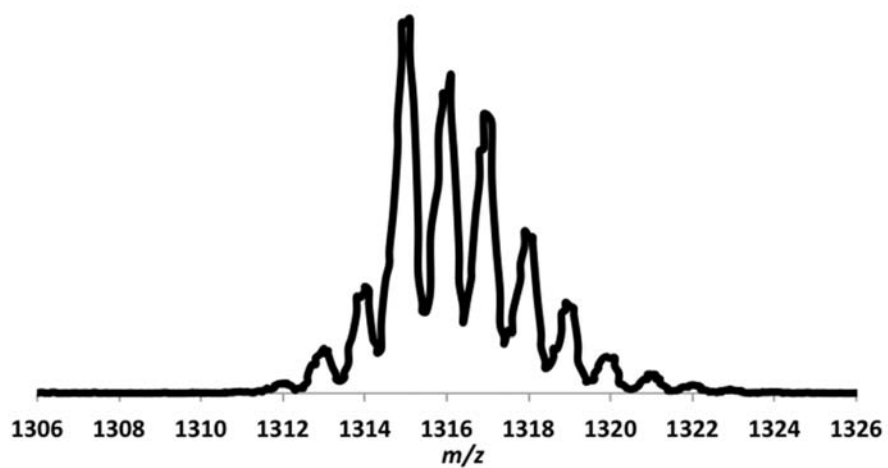
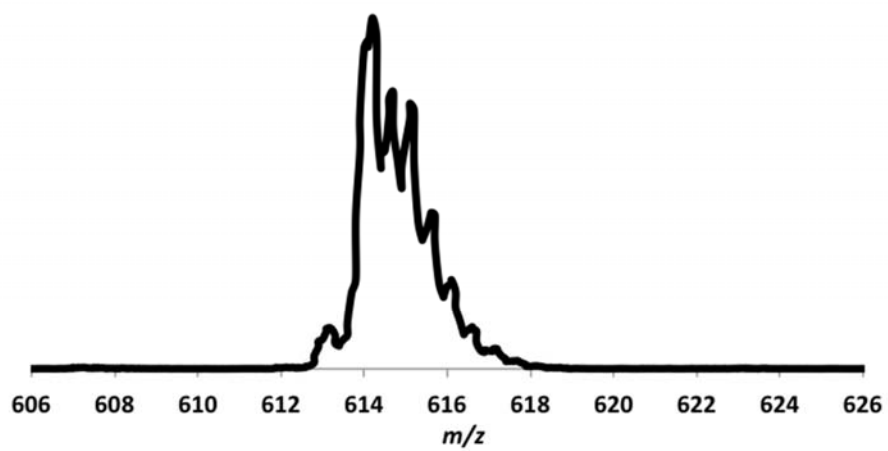


Figure S20: Positive ion ESI mass spectra of $[1c](BF_4)_2$.

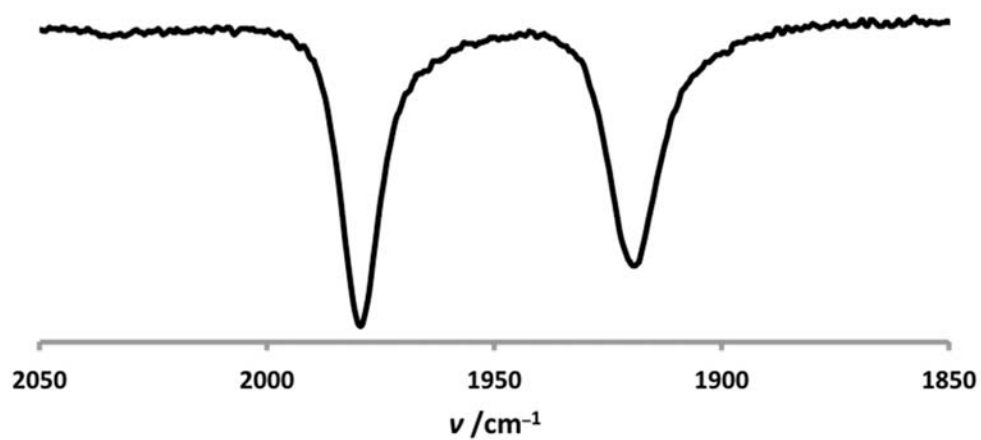


Figure S21. FT-IR spectrum (ν_{CO} region, CH_2Cl_2) of $[\mathbf{2a}]\text{BF}_4$.

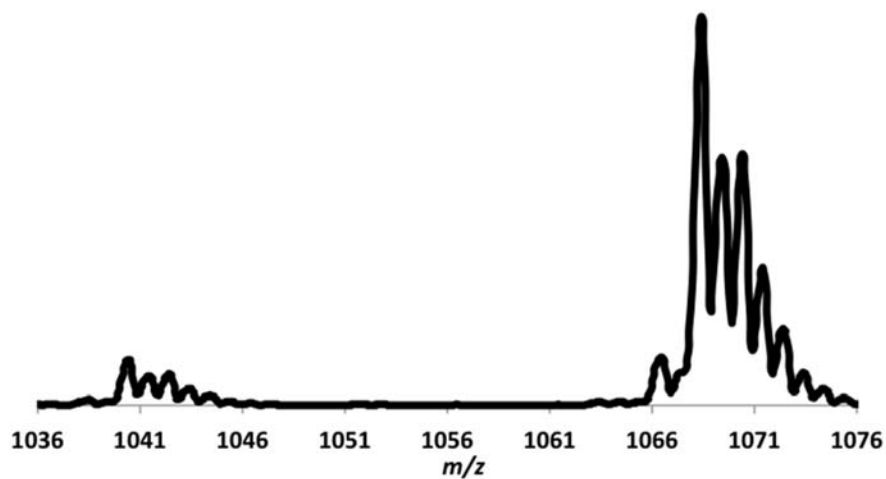


Figure S22. Positive ion ESI mass spectrum of $[\mathbf{2a}]\text{BF}_4$.

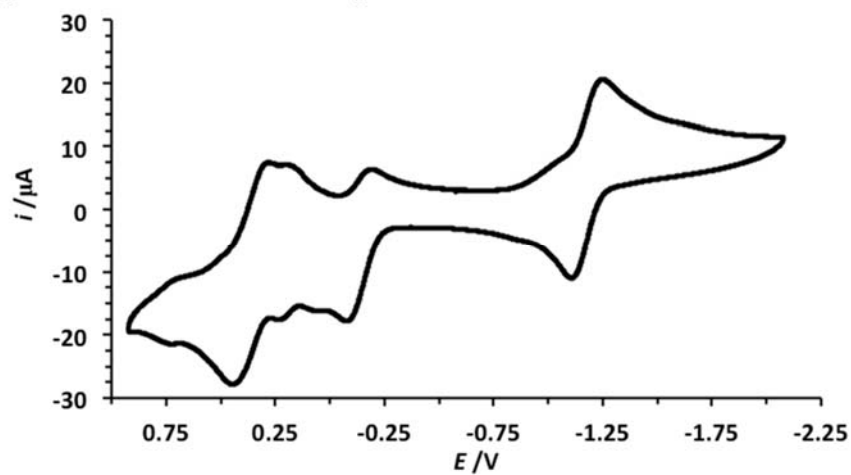


Figure S23. Cyclic voltammogram of $[\mathbf{2a}]\text{BF}_4$.

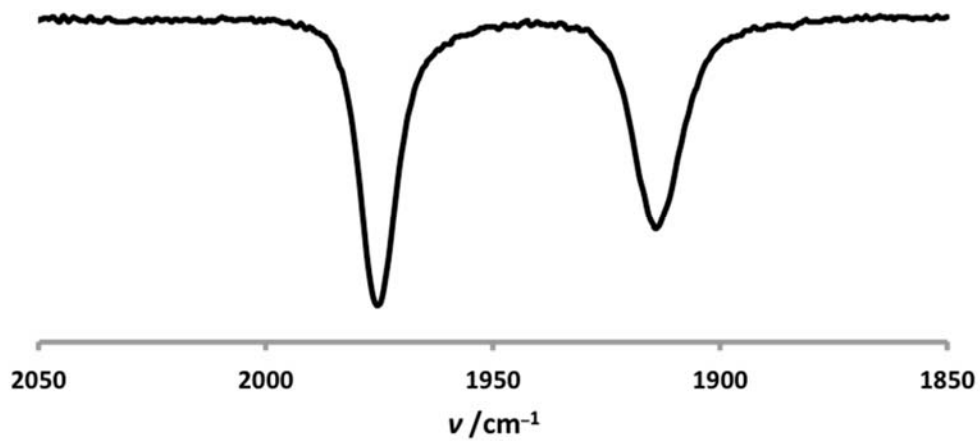


Figure S24. FT-IR spectrum (ν_{CO} region, CH_2Cl_2) of **[2b]** BF_4 .

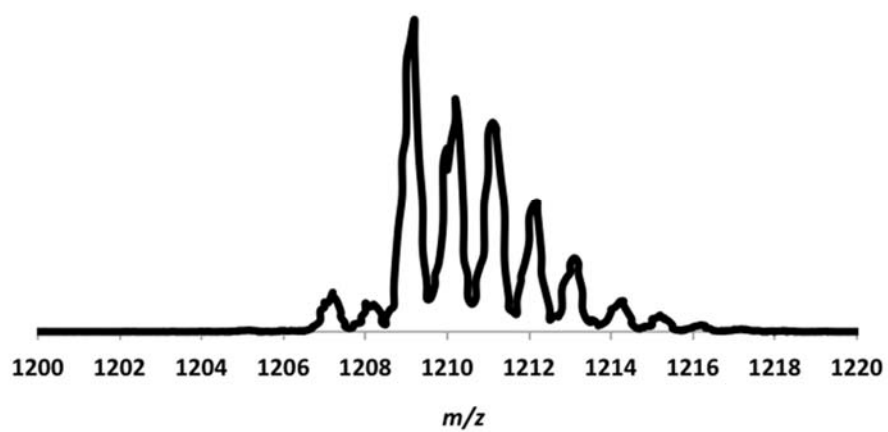


Figure S25. Positive ion ESI mass spectrum of **[2b]** BF_4 .

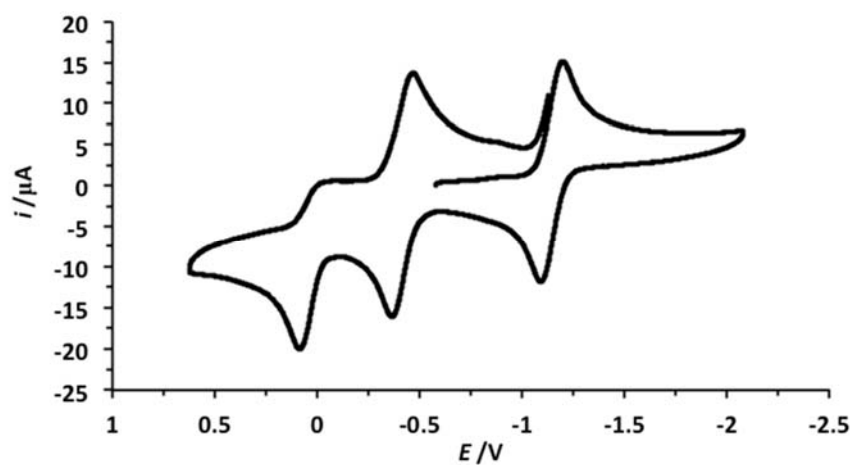


Figure S26. Cyclic voltammogram of [2b]BF₄.

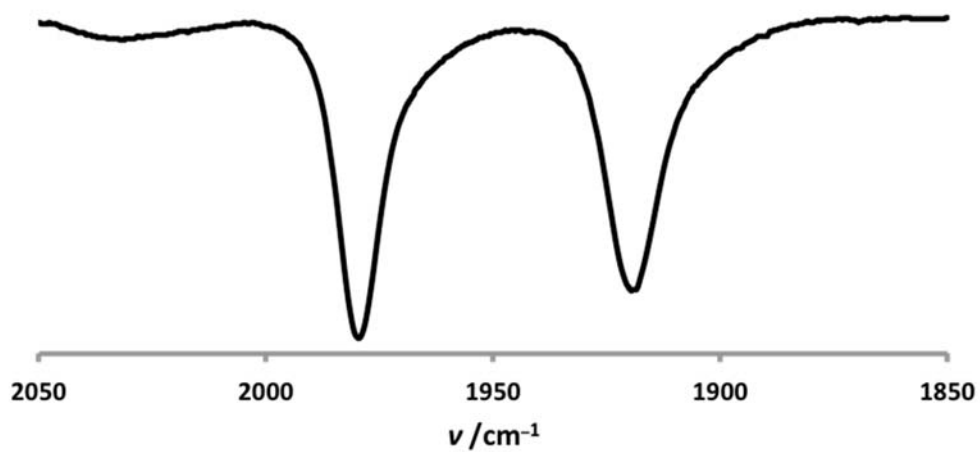


Figure S27: FT-IR spectrum (ν_{CO} region, CH₂Cl₂) of [2c]BF₄.

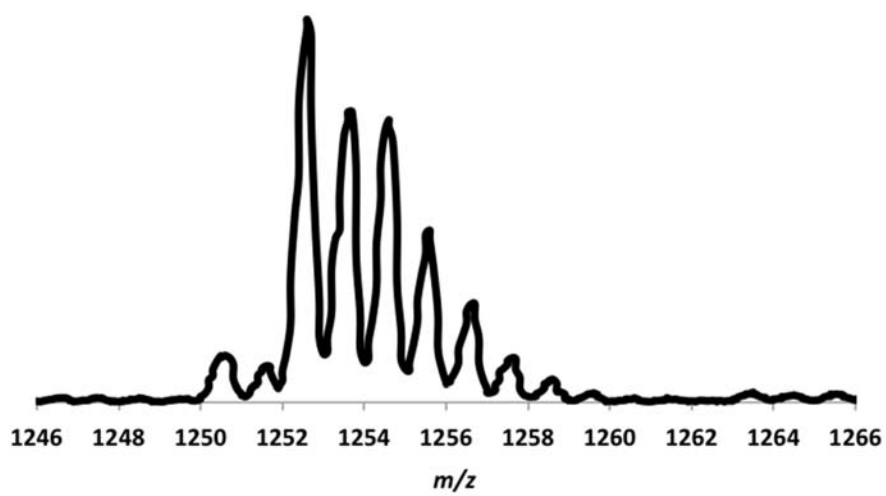


Figure S28. Positive ion ESI mass spectrum of [2c]BF₄.

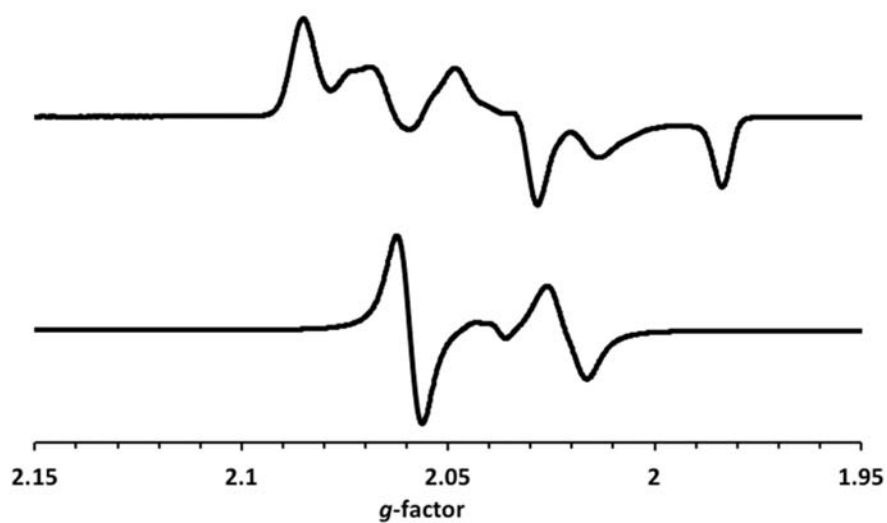


Figure S29. X-band EPR spectra of [2c]BF₄ in CH₂Cl₂/PhMe recorded at 110 K (top) and room temperature (bottom).

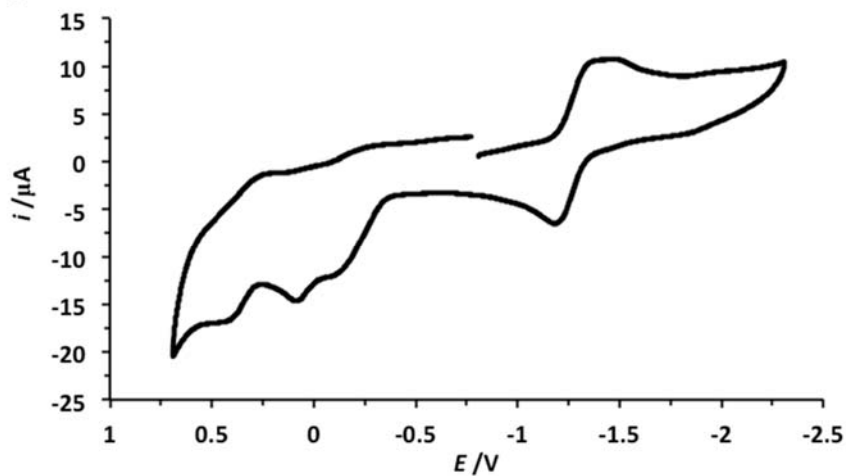


Figure S30. Cyclic voltammogram of [2c]BF₄.

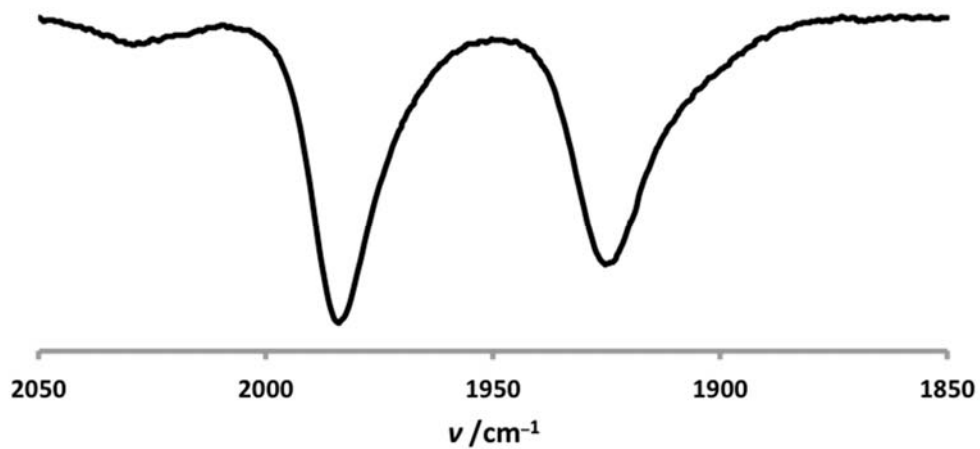


Figure S31: FT-IR spectrum (ν_{CO} region, CH_2Cl_2) of $[\mathbf{3}](\text{BF}_4)_2$.

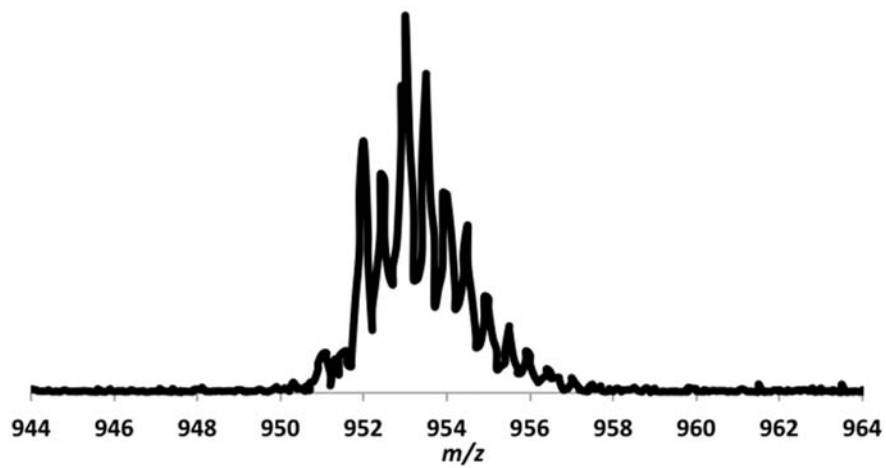


Figure S32. Positive ion ESI mass spectrum of $[\mathbf{3}](\text{BF}_4)_2$.

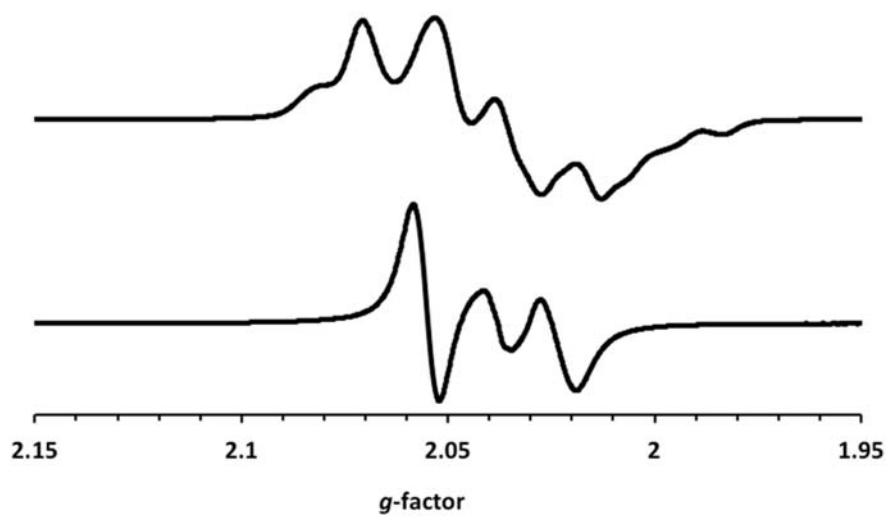


Figure S33. X-band EPR spectra of $[3](BF_4)_2$ in $CH_2Cl_2/PhMe$ recorded at 110 K (top) and room temperature (bottom).

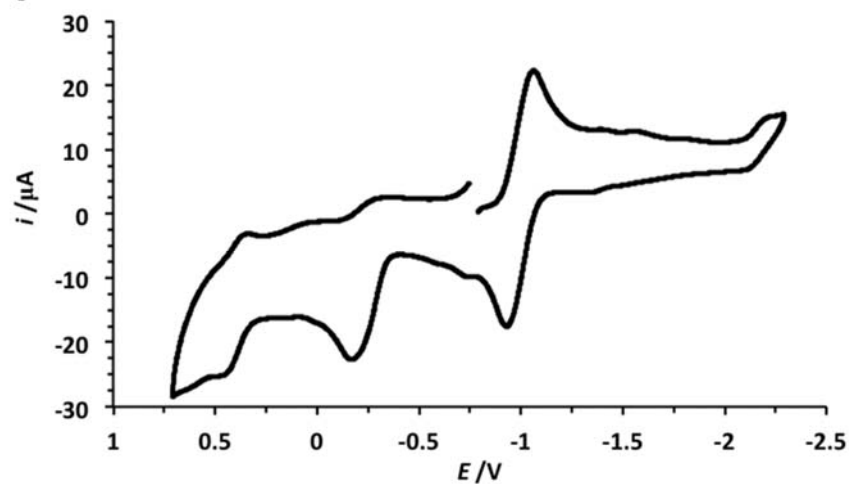


Figure S34. Cyclic voltammogram of $[3](BF_4)_2$.